Analytical and Numerical Evaluations of Flexible V-Band Rotman Lens Beamforming Network Performance for Conformal Wireless Subsystems

Ardavan Rahimian*, **Yasir Alfadhl, and Akram Alomainy**

Abstract—This paper presents the analytical design and numerical performance evaluation of novel V-band millimetre-wave (mm-wave) beamforming networks (BFNs), based on the Rotman lens array feeding concept. The devices are intended for operation in the unlicensed 60-GHz frequency band. The primary objective of this work is to study the feasibility of designing flexible V-band beamformers, based on liquid-crystal polymer (LCP) substrates. The planar Rotman lens device has been initially developed, and the output performances, in terms of the scattering parameters and accuracy, have been analysed. This is further continued with the detailed designs of the Rotman lens BFNs based on the four different proposed flexural cases, namely the concave-axial bending, the convex-axial bending, the concave-circumferential bending, and the convex-circumferential bending. Each of the flexures has been analysed, and the performance in terms of the surface currents and phase distributions, as the primary functionality indicators, has been presented. The presented flexible beamformers exhibit significant characteristics to be potentially employed as low-cost and efficient units of the mm-wave transceivers with the in-built electronic beam steering capabilities for the conformal wireless subsystems.

1. INTRODUCTION

The intrinsic structural geometries of the advanced flexible microwave and mm-wave components, antennas, and electromagnetic (EM) systems are conformed to particular surfaces, including cylindrical, spherical, and conical shapes. This unique feature enables compliance of the radio frequency (RF) systems with various state-of-the-art requirements to extend both the aerodynamic and hydrodynamic properties of the intended platforms. This is also crucial for modern wireless communication systems, such as the fifth generation (5G) wireless networks [1–3]. These flexible components, with their practical characteristics and manufacturing processes, are able to expand and enhance the system functionalities, in terms of wideband operation and electronic beam steering. Furthermore, these devices introduce the integrability with existing installed elements of the core network infrastructure [4–6], as in the base transceiver station (BTS) and wireless backhaul architectures, in which the other structures have limitations and certain drawbacks [7].

On the other hand, the rapid increase in the data traffic volume and the enormous usage of smart devices have already initiated the deployment of the wireless systems for operation in the mm-wave spectrum. The range is considered as a potential candidate for the provision of the high-capacity channels (i.e., multi-Gbps), and the efficient exploit of the RF links and access technologies for the short- and mid-range high-speed and high date rate communications with indoor and outdoor interconnections [8–10]. For this reason, the V-band unlicensed 60-GHz frequency range is a promising

deployment solution for these types of communications, due to the 7-GHz of available EM spectrum, with the suitability for the establishment of the secure links, along with the frequency reuse [11]. However, the intended band exhibits a number of challenges for the efficient utilisation, including the path loss due to the atmospheric absorption caused by the gases and precipitation [12]. This further implies a substantial need for the employment of the beamformers in order to maintain the link budget requirements [13], for both the line-of-sight (LoS) and non-line-of-sight (NLoS) communication scenarios, and to compensate for the path losses in the RF channel, resulting in the overall mm-wave quality enhancement [14].

The fields of microwave and mm-wave BFNs incorporate mainly two types of RF feeding systems, namely circuit-based beamformers and lens-based ones, in order to generate multiple independent beams that are focused at different directions [15]. The Rotman lens [16–19], as a cost-effective and high-performance beamformer with the true-time-delay (TTD) switched-beam capabilities, realises linear phase progression with appropriate amplitudes, exciting consecutive radiating elements within an array. This results in the signal-to-noise ratio (SNR) improvement and in the co-channel interference (CCI) reduction, by pointing the directional beams to the desired spatial directions and enforcing nulls for the set of undesired ones [20]. Hence, in order to provide both the extended range and angular coverage, along with the adaptation to enable the spatial multiplexing, the feasirity analysis of the beam steering based on the advanced flexible mm-wave components is essential. This investigation is of vital importance in order to have control over the amplitude and phase at each element of the array, for the RF module integration at the network access point (NAP) level.

The remainder of this paper is organised as follows. Section 2 presents the analytical modelling and evaluation of the Rotman lens (RL) device, along with the discussion of the planar structure. In Section 3, the proposed flexible BFNs, along with the analysis and efficiency evaluation of the output performances, are presented (i.e., to the best of the authors' knowledge, this is the first attempt in order to design and analysis of such flexible mm-wave array beamforming networks). The paper is concluded in Section 4.

2. THEORETICAL DESIGN AND ANALYSIS

2.1. Analytical Modelling and Evaluation

The Rotman lens is an efficient high-performance feeding network due to its low-cost, reliability, and wide scanning capabilities. It avoids the complexities of phase shifters to steer an RF beam over wide angles and has proven itself to be a useful beamformer for electronically scanned arrays (ESAs) [19]. It produces RF beam scanning independent of the frequency and is, therefore, capable of wideband operation [21]. The Rotman lens, as a constrained lens-based device, in which an EM wave is guided along the constrained paths upon the design equations, which generates multiple beams with specific magnitude and phase characteristics, is able to provide the required functionalities for the wireless subsystems. It has a carefully designed structure and appropriate-length transmission lines to produce a wave-front across the output that is phased by the time-delay in the transmission [22]. Each input port will produce a distinct beam that is shifted in angle at the output. The design of the RL is controlled by a series of equations that set the focal points and array positions. The inputs include the desired scan angle of the array, the operating frequency, the number of beams and array ports, and the array element spacing. The geometry optimisation, phase error and coupling analysis are also considered while designing the device, as thoroughly discussed in [23–26]. For the sake of brevity, the design equations are not provided.

In this section, the analytical computation and modelling regarding the scattering matrix has been conducted in detail, based on applying the equivalence principle, in which the port aperture is replaced by the equivalent electric and magnetic surface currents (i.e., generation of the fields within the lens cavity) that are linearly related to the port current (i.e., flowing toward the lens cavity), and the port voltage, as in Eqs. (1) and (2). Also, V_1, V_2, ..., V_N and I_1, I_2, ..., I_N are considered as the port voltages and currents, respectively, with the N as the total number of ports, including the beam, array, and dummy ports [27]. The reflections are calculated based on the incident ray, which is reflected on

the path to the receiving port, according to the properties of the dummy port's boundary.

$$\overset{\text{def}}{=} \begin{cases} \hat{z}I_{sp} = -\hat{z}\frac{I_p}{W_p} \\ \hat{t}_pM_{sp} = \hat{t}_p\frac{V_p}{h} \end{cases} \xrightarrow{yields} E_z(x,y) = \sum_{p=1}^{N} I_pE_{zp}^I\left(x,\frac{y}{x_p},y_p\right) + V_pE_{zp}^M\left(x,\frac{y}{x_p},y_p\right); \tag{1}$$

$$\xrightarrow{yields} V_q = -hE_z(x_q,y_q) = -h\sum_{p=1}^{N}\left[I_pE_{zp}^I\left(x_q,\frac{y_q}{x_p},y_p\right) + V_pE_{zp}^M\left(x_q,\frac{y_q}{x_p},y_p\right)\right]; \quad q=1,2,\ldots,N. \tag{2}$$

where Wp is the width of the pth port of the lens; h is the port height (i.e., the distance between the centre conductor and the lower ground plane); E_{zp}^I and E_{zp}^M are the electric fields at the coordinate (x, y), with (x_p, y_p) as the midpoint, generated by the pth port electric and magnetic currents, respectively; $\hat{z}$ and $\hat{t}_p$ are the unit-vectors perpendicular to the cavity plane and along the contour, respectively. As the equations present, the total field within the lens cavity is obtained, which leads to the voltage V_q at the qth port.

$$\overset{\text{def}}{=} [A][V] = [B][I] \xrightarrow{yields} [Z] = [A]^{-1}[B]; \quad \rho_{qp} = \sqrt{(x_q-x_p)^2 + (y_q-y_p)^2}. \tag{3}$$

$$a(q,p) = \delta_{pq} + hE_{zp}^M\left(x_q,\frac{y_q}{x_p},y_p\right) \approx j\frac{W_p}{4}k\frac{y_q-y_p}{\rho_{qp}}H_1^{(2)}(k\rho_{qp}); \tag{4}$$

$$b(q,p) = -hE_{zp}^I\left(x_q,\frac{y_q}{x_p},y_p\right) \approx \frac{\omega\mu h}{4}H_0^{(2)}(k\rho_{qp}). \tag{5}$$

The derived expressions are then rearranged as in Eq. (3), to build up the constituent matrix, with $[A]$ and $[B]$ as the $N \times N$ square matrices, and $[V]$ and $[I]$ as the column vectors of order N. The impedance matrix $[Z]$ is obtained, incorporating the elements of $[A]$ and $[B]$. As presented in [27], the spectral domain analysis, based on the Galerkin's method of moments (MoM) formulation with subdomain basis functions, is further computed in order to obtain the fields in the isotropic and homogeneous medium; therefore, resulting in the derived deduced asymptotic expressions of Eqs. (4) and (5), with $H_n^{(2)}$ as the Hankel function of the second kind of order. The scattering matrix elements therefore present the coupling between the ports (i.e., when all ports are match-terminated) and further employed in order to check the consistency of the scattering solution, with respect to a given port, based on the z-component of the electric field.

## 2.2. Planar Design and Evaluation

In the development of the flexible and conformable high-frequency components, substrate materials are crucial to the deployment of the low-cost and power-efficient broadband wireless systems [28, 29]. In this regard, Rogers ULTRALAM 3850HT liquid-crystal polymer (LCP) flexible and recyclable laminates exhibit significant combination of the electrical, thermal, chemical, and mechanical properties, for the improved construction of the high-speed mm-wave devices and systems at higher temperatures (i.e., the permeation of gases through the material is not affected by the humidity) [30–33]. The LCP material has low moisture absorption and can also withstand chemical exposure, as well as temperature variations, and further exhibits dielectric constants of 2.9–3.1 and loss tangent less than 0.005, throughout the RF range up to 110-GHz, with a substrate thickness of 100 μm [34]. These unique features make the LCP substrate very appealing as a primary enabling technology for the potential multi-environmental wireless applications.

The EM simulations regarding the design of the planar V-band lens have been carried out, and the output characteristics, including the beam to array coupling amplitudes, and the return and insertion losses, have been presented for the operating frequency band (i.e., Fig. 1). The lens has been developed based on the 5×8 configuration, in which the LCP-based beamformer incorporates five input (i.e., beam) ports and eight output (i.e., array) ports, suitable for an eight-element array, along with eight dummy ports, to absorb the energy and to reduce the reflections on each side of the lens cavity. The device has the scan angle of $\pm 30°$ with the half-wavelength array element spacing. The designed lens has the structure that connects the beam contour to the output array contour for the

optimum power distribution across the array ports, along with the linear phase progression among the adjacent elements. As Fig. 1 shows, the RL has been implemented based on the LCP substrates with different configurations and curvatures, namely the square-shaped substrate, edge-shaped substrate, and extrusion-shaped substrate. These substrates incorporate the copper layers for the lens and ground planes at the top and bottom of the component, respectively, in order to assess the effects of the introduced configurations on the performances. The parameters have been examined according to the observed variations in the S-parameters, consequently in the device efficiencies, based on the excited beam ports. The results further confirm an almost uniform behaviour among the lenses with the different substrate configurations. This process can facilitate the analysis of the system interaction in the case of the active and passive components' presence within a module for the integration purposes, as in the embedded systems development (ESD).

Furthermore, Fig. 2 presents the surface current distributions of the planar LCP-based Rotman lens for the activated input beam ports one to five. As Fig. 2 shows, the maximum power is delivered to the output array elements, and the progressive surface currents confirm the high-performance operation of the device. The lens efficiently conducts the EM energy distributions across the array ports, effectively resulting in the provision of the electronic beam scanning functionality for the utilisation of the wireless subsystems.

The comprehensive full-wave EM simulations have been carried out in order to analyse the characteristics of the proposed designs. Fig. 3 indicates the S-parameters' magnitudes for the device with beam ports one to three excited. Because of the intrinsic symmetrical structure of the lens, the performances of beam ports one and two are theoretically identical to the performances of beam ports five and four, respectively. The magnitudes have low-ripples (i.e., less than 6 dB) over the intended

(a)   (b)   (c)
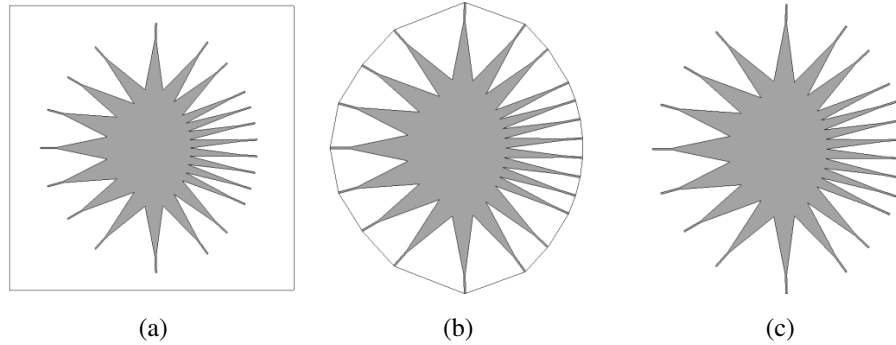
Figure 1. Simulated planar V-band LCP-based Rotman lens beamformer devices with four beam ports, eight array ports, and eight dummy ports, with core lens dimensions of 38.12 mm × 43.86 mm: (a) RL-BFN-I: the square-shaped substrate configuration; (b) RL-BFN-II: the edge-shaped substrate configuration; (c) RL-BFN-III: the extrusion-shaped substrate configuration.

(a)   (b)   (c)   (d)   (e)
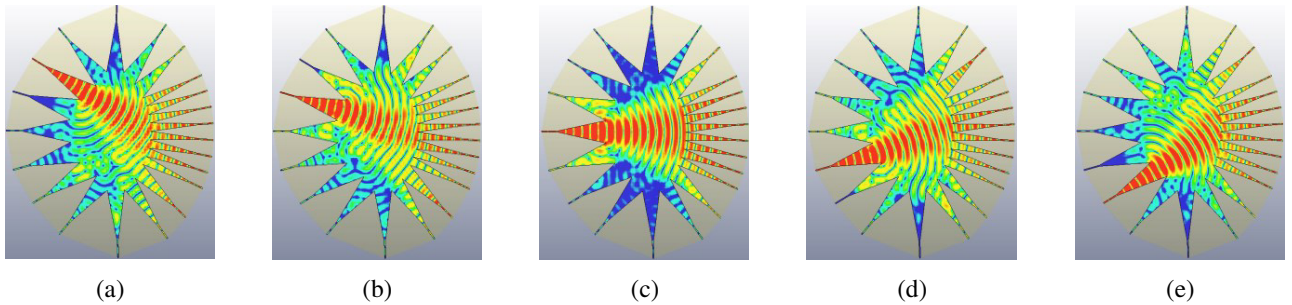
Figure 2. Surface current distributions of the planar V-band LCP-based Rotman lens BFN, for the excited input ports: (a) beam port one active; (b) beam port two active; (c) beam port three active; (d) beam port four active; (e) beam port five active.
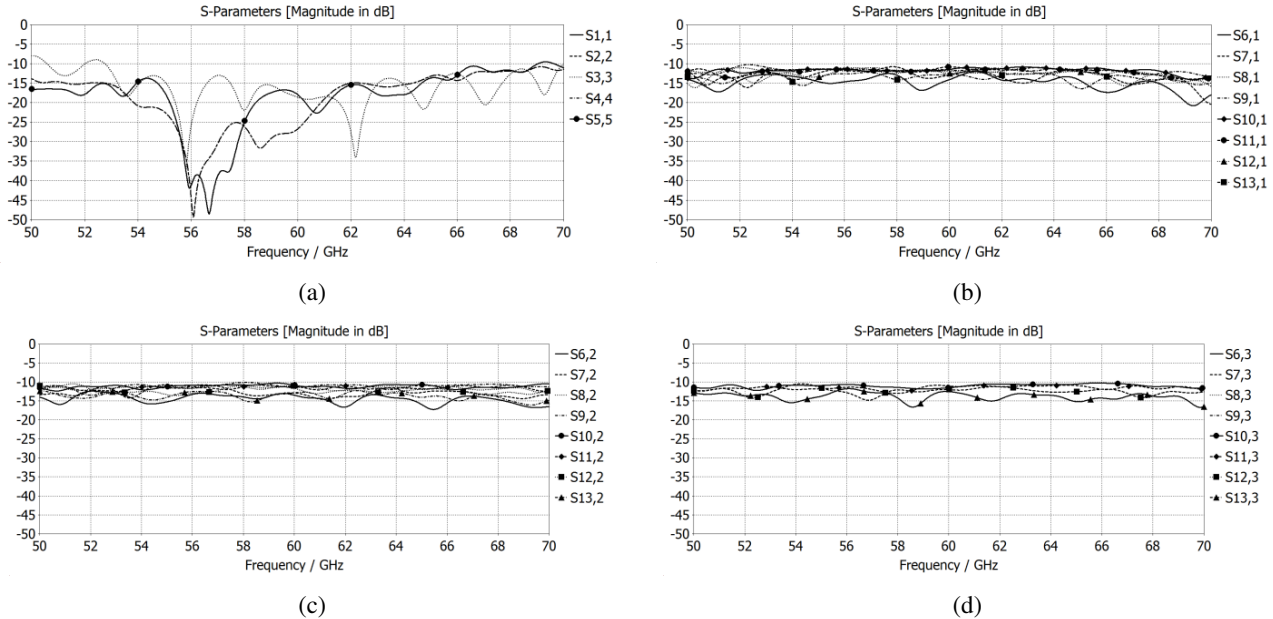
Figure 3. Simulated S-parameters of the planar V-band LCP-based 5×8 Rotman lens BFN for the wideband operation: (a) return loss plots for input beam ports one to five active; (b) insertion losses for input beam port one active; (c) insertion losses for input beam port two active; (d) insertion losses for input beam port three active.
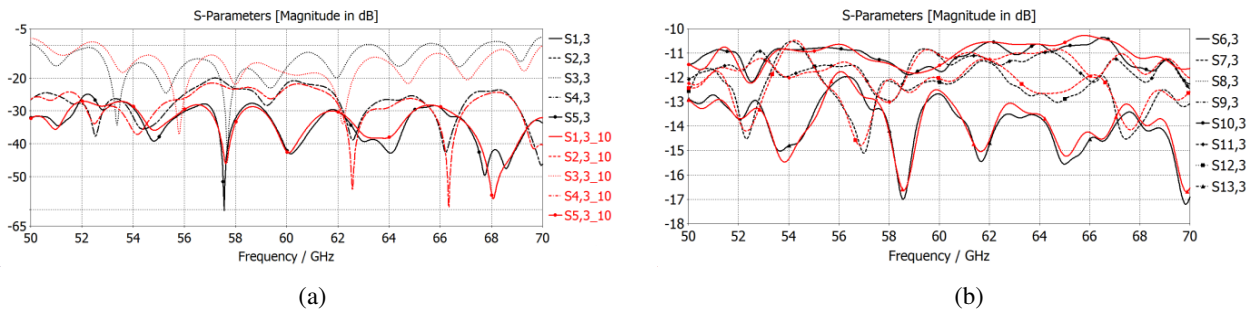
Figure 4. Comparison of the simulated output characteristics for the excited beam port three, based on the two different numerical mesh-discretisation resolution cases: (a) return losses and adjacent input beam port isolations; (b) insertion losses of the lens.

V-band frequency range, exhibiting almost linear distributions across the array ports. The simulated S-parameters of the designed lens confirm the wideband operation of the device and further realise the output performance based on the behavioural conformity according to the generalised RL theory. The generation of the RF beams in different orientations results in the provision of the hybrid versatility and robustness in the Gbps communications, along with the optimised and symmetrical radiation patterns, in response to the RF propagation environment in the imperfect mm-wave channels encountering the multipath, interference, and fading, for the efficient deployment of the RF modules.

Moreover, as Fig. 4 shows, an extra analysis has been conducted for port three, based on the increased numerical discretisation's resolution, to assess accuracy of the simulations, and to examine the margin of error using the software. This process has resulted in the increased level of precision for the verification and comparison of the results, and can be used in the RF sensitivity assessments based on the specified background materials, permittivity values, and EM boundary conditions. Fig. 4 shows the output characteristics of the RL for the excited beam port three, based on the mesh-discretisation with the 20 lines per wavelength. As can be seen from the S-parameters' magnitude plots, the device

still conforms to the expected RF behaviour, in both the applied high-resolution EM cases (i.e., the 10 and 20 lines per wavelength), that have resulted in the presented return loss and adjacent input beam port isolations (i.e., $S_{1,3}$ to $S_{5,3}$) and insertion losses (i.e., $S_{6,3}$ to $S_{13,3}$), for the demonstrated planar V-band LCP-based Rotman lens beamformer.

## 3. DESIGN AND ANALYSIS OF FLEXIBLE BEAMFORMING NETWORKS

This section presents the design and analysis of the V-band flexible BFNs, in order to precisely investigate the feasibility of the flexural functionality, introduced intrinsically into the case of Rotman lens. The complex EM simulations have been carried out for the RL structures with the specific flexural degrees, based on the four different flexural cases (i.e., Fig. 5). Furthermore, the thoroughly high-performance computing (HPC)-based simulations for the surface current distributions and phase behaviour, along with the numerical device efficiency analysis, as the primary indications of the high-performance mm-wave operation, have been conducted for each flexural case. Fig. 5 shows the V-band beamforming networks based on the four unique flexures, namely the concave-axial bending, convex-axial bending, concave-circumferential bending, and convex-circumferential bending. Furthermore, their individual characteristics, in terms of the surface currents and phase distributions, are presented in the following sections. The performances of the BFNs conform to the deployment requirements of the advanced wireless communication systems and can be further integrated with the radiating elements in order to build up the flexible modules for the potential hybrid wireless applications, such as the conformal backhaul subsystems. The proposed mm-wave beamforming networks can also be employed for the potential implementation of the retrodirective systems, as in [35]. In this case, the characteristics of the devices enable the generated RF beams to be received from specific directions and to be further transmitted back to the same sources without physical arrangements, in order to realise the intelligent beam alignment functionalities. This kind of electronic scanning is faster than the conventional methods and provides the feasibility for the implementation of smart systems, in which the EM patterns are changed according to the RF propagation environment, that further offer impressive properties, including the ultimate performance in terms of the signal quality, interference- and noise-suppression, and information capacity.

(a) (b) (c) (d)
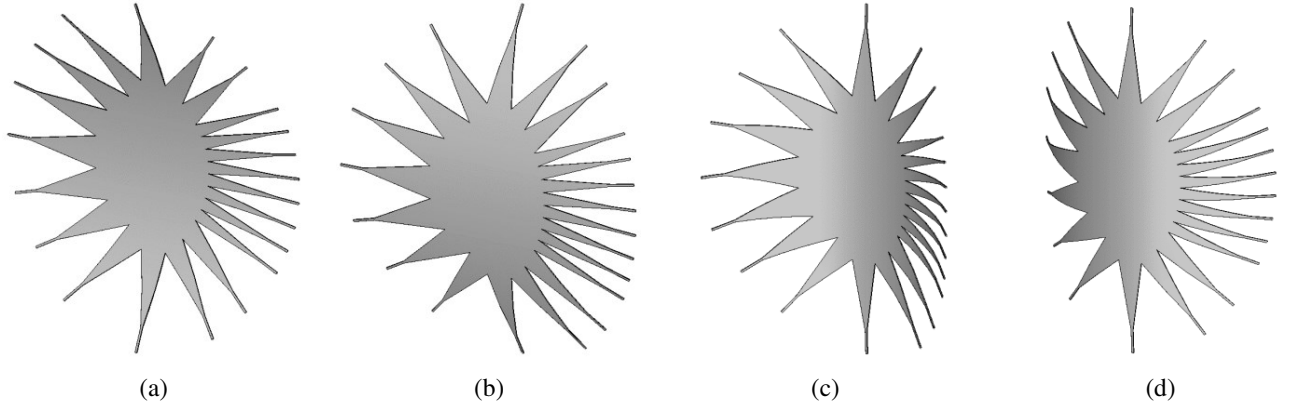
Figure 5. Perspective views of the proposed flexures based on the designed V-band 5×8 Rotman lens BFNs: (a) the concave-axial bending; (b) the convex-axial bending; (c) the concave-circumferential bending; (d) the convex-circumferential bending.

3.1. Flexural Case-I: The Concave-Axial Bending

Figure 6 presents the surface current distributions for the V-band Rotman lens based on the first flexural case (i.e., the concave-axial bending), along with the corresponding linear phase behaviour, for the excited beam ports one and three, as the primary functionality indicators. It is worth noting that beam ports one and five determine the minimum device efficiency, since they are symmetrical on both ends of the lens and are placed on the furthest distance from the central focal point of the device. The
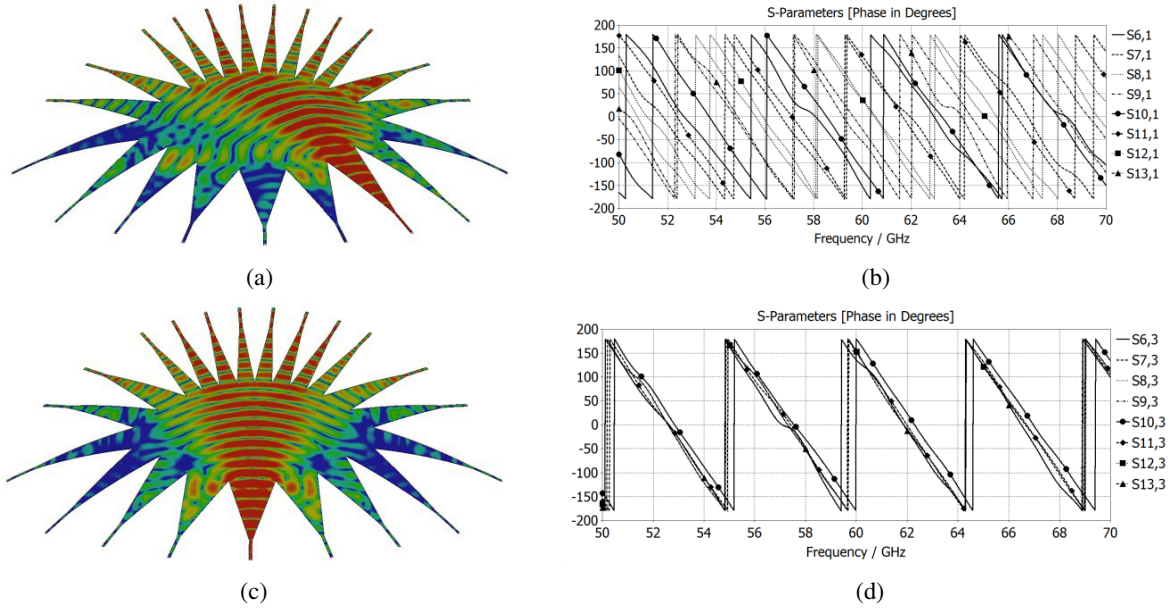
Figure 6. RF performance characteristics of the V-band LCP-based RL based on the flexural case of the concave-axial bending, in which the device is bent around a cylinder of radius $R = 40$-mm: (a) surface current distributions for beam port one active; (b) linear phase distributions for beam port one active; (c) surface current distributions for beam port three active; (d) linear phase distributions for beam port three active.

activated beam port three exerts the maximum efficiency into the component, since it is placed on the central axis. Hence, the device efficiency can be expressed as the sum of the absolute squares of the output array ports' linear transmission coefficients, as derived in Equations (6)–(8), where n and m refer to the array and beam ports, respectively. Each set of parameters indicate different results, from which the device efficiency is determined. As Figs. 6(a) and (c) present, the surface current distributions confirm the efficient power division along the array ports of the component, and further confirming the linear phase distributions required for the mm-wave beam steering, in Figs. 6(b) and (d). The minimum and maximum device efficiencies at the centre frequency of 60-GHz for the excited beam ports one and three are numerically obtained as 47.1% and 51.7%, respectively, based on the presented device efficiency equations.

$$\stackrel{\text{def}}{=} Eff_{\min} = \frac{P_{RL_{out}}}{P_{RL_{in}}} = \sum_n |S_{n,1}|^2 = \left(S_{6,1}^2 + S_{7,1}^2 + S_{8,1}^2 + S_{9,1}^2 + S_{10,1}^2 + S_{11,1}^2 + S_{12,1}^2 + S_{13,1}^2\right). \quad (6)$$

$$\stackrel{\text{def}}{=} Eff_{\max_{odd(m)}} = \frac{P_{RL_{out}}}{P_{RL_{in}}} = \sum_n \left|S_{n,\frac{m+1}{2}}\right|^2 = \left(S_{6,3}^2 + S_{7,3}^2 + S_{8,3}^2 + S_{9,3}^2 + S_{10,3}^2 + S_{11,3}^2 + S_{12,3}^2 + S_{13,3}^2\right). \quad (7)$$

$$\stackrel{\text{def}}{=} Eff_{max_{even(m)}} = \frac{P_{RL_{out}}}{P_{RL_{in}}} \stackrel{yields}{\longrightarrow} \sum_n \left|S_{n,\frac{m}{2}}\right|^2 and \sum_n \left|S_{n,\frac{m}{2}+1}\right|^2. \quad (8)$$

3.2. Flexural Case-II: The Convex-Axial Bending

This section presents the characteristics of the designed flexible Rotman lens based on the flexure of the convex-axial bending. Fig. 7 shows the surface current distributions for the excited beam ports one and three, corresponding to the exertions of the minimum and maximum device efficiencies, respectively. The linear phase distributions based on the activated ports are shown in Figs. 7(b) and (d), in order to present the RF beam steering in terms of the required phase behaviour. Hence, multiple beams without the need for phase shifters have been generated, based on the proposed RF component with
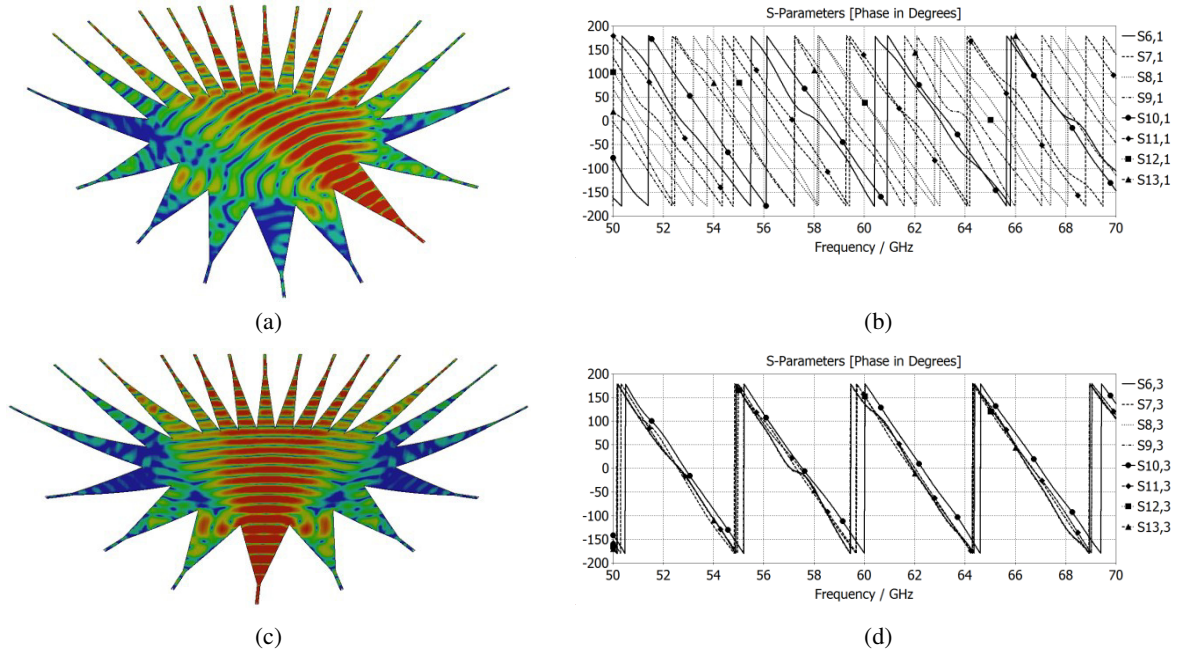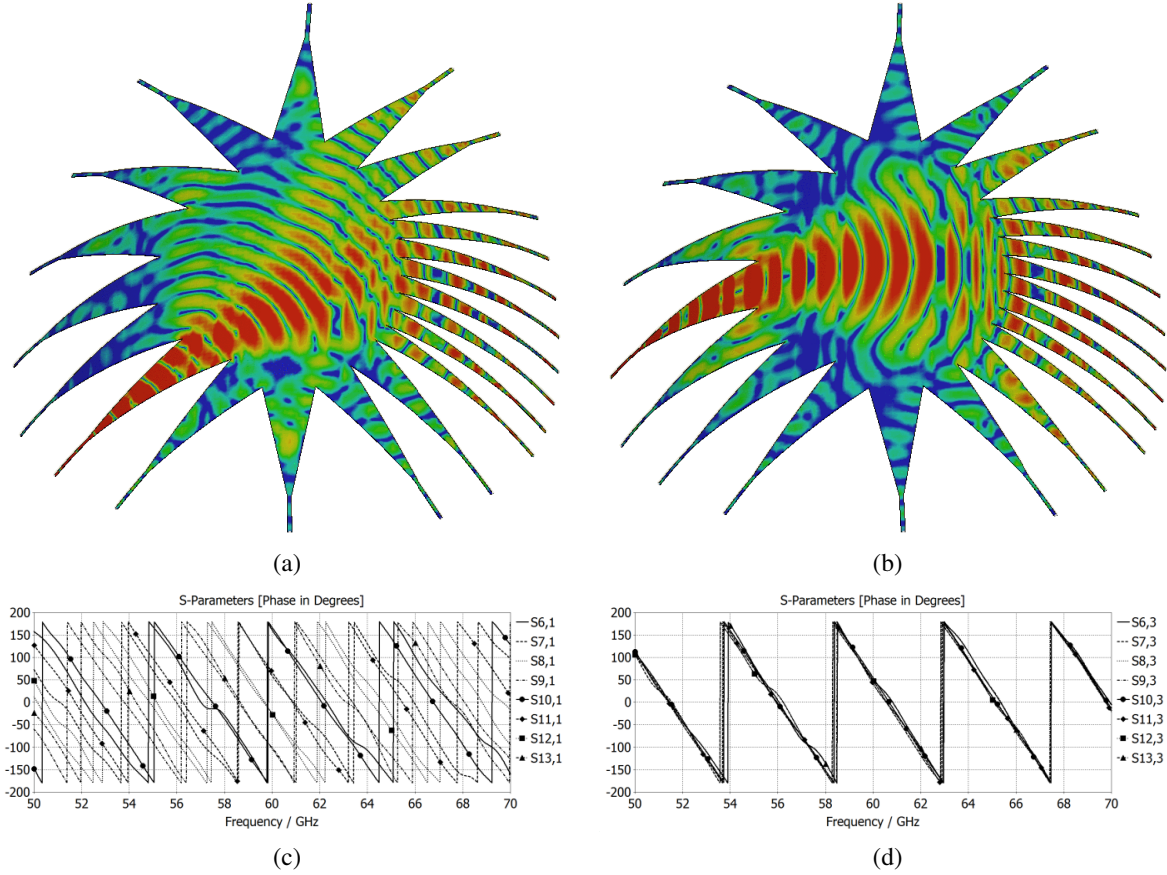
Figure 7. RF performance characteristics of the V-band LCP-based RL based on the flexural case of the convex-axial bending, in which the device is bent around a cylinder of radius $R = 40$-mm: (a) surface current distributions for beam port one active; (b) linear phase distributions for beam port one active; (c) surface current distributions for beam port three active; (d) linear phase distributions for beam port three active.

the wideband operation and wide angle scanning capabilities. All the generated beams can be used simultaneously or can be switched at high rates, which results in the pattern diversity for the potential wireless multiple-input multiple-output (MIMO) systems, in which an extra radio at each beam port can be further integrated for the hybrid mm-wave module development. The minimum and maximum device efficiencies are obtained as 47.8% and 51.7% for the excited beam ports one and three, respectively. The flexible lens can be extensively employed as a subsystem core of the requirements for the backhaul infrastructures. The device can be integrated with the systems where the high-capacity and reliable data transmission, based on the implemented components and adaptive processing, are of critical demand among the NAPs, in order to effectively maintain the RF beam steering functionality based on the advanced low-cost and lightweight mm-wave modules.

3.3. Flexural Case-III: The Concave-Circumferential Bending

This section shows the performance of the proposed mm-wave component based on the third flexural case, in which the V-band LCP-based beamformer is bent around a cylinder to form the structure of the concave-circumferential bending. Hence, Fig. 8 shows the characteristics of this flexure, for the excited ports one and three. As Figs. 8(a) and (b) present, the surface current distributions throughout the lens confirm the efficient EM energy distribution along the array ports, with the maximum and minimum intensities being appropriately delivered to the array ports and dummy ports, respectively. As Figs. 8(c) and (d) show, phase behaviour of each individual excited port further confirms the linear distributions required for the systematic mm-wave beam scanning functionality. The minimum and maximum device efficiencies, for the excited ports one and three at the centre frequency of 60-GHz, are numerically computed as 45.8% and 54.2%, respectively. The Rotman lens is operative based on the TTD functionality, and as expressed in (9), when the lens is switching between the input ports, the radiated beam can be scanned through the field of view (FOV) of the device, in order to achieve a high angular resolution through the progressive linear time-delay (i.e., denoted by $\Delta\tau$) across the array elements. This further results in the constructive interference, along with the delay between

Figure 8. RF performance characteristics of the V-band LCP-based RL based on the flexural case of the concave-circumferential bending, in which the device is bent around a cylinder of radius $R = 20$-mm: (a) surface current distributions for the excited port one; (b) surface current distributions for the excited port three; (c) linear phase behaviour for the excited port one; (d) linear phase behaviour for the excited port three over the central axis, incorporating the elements of the central beam of the array factor (AF).

the adjacent elements with the constant separation (i.e., denoted by D) that generates the radiation pattern relative to the central axis of the component. Therefore, as Equation (9) depicts, where c is the speed of light and θ_s the scan angle, the RL-BFN is the TTD device, which further confirms that the beam scan angle depends solely on the time-delay, since in the TEM-based transmission mediums, $\Delta\tau$ is frequency-independent. Hence, the scan angle does not vary with the frequency, which enables the provision of RF features to be exploited for the conformal wireless applications [36].

$$\xrightarrow{TTD} \theta_s = \sin^{-1}\left(\frac{c\Delta\tau}{D}\right). \tag{9}$$

3.4. Flexural Case-IV: The Convex-Circumferential Bending

Figure 9(a) shows the surface current distributions for the device based on the flexural case of the convex-circumferential bending with beam port one active, along with the corresponding linear phase behaviour, as presented in Fig. 9(c). Also, Fig. 9(b) shows the surface current distributions in the case of the maximum efficiency's exertion based on the excited port three, which is followed by its linear phase behaviour, as shown in Fig. 9(d). The minimum and maximum device efficiencies at the centre frequency of 60-GHz for the excited ports one and three are 46.6% and 54.8%, respectively. The device is bent under the extreme flexure as well, in order to examine the performance of the BFN under this

condition. Fig. 9(e) indicates the flexural structure under the extreme bending, in which the lens is bent around a cylinder with the R_2 radius. Fig. 9(f) shows the output in terms of the surface currents, which depicts the efficient distribution along the array ports. Also, the EM range indicates the intensities throughout the component. This scale has been set for the other flexures as well, in order to deploy a uniform EM range among the proposed flexures. The device efficiency for this extreme case, in which only beam port three is excited for the maximum efficiency's exertion, is computed as 53.1%.

(a)

(b)

(c)

(d)

(e)

(f)
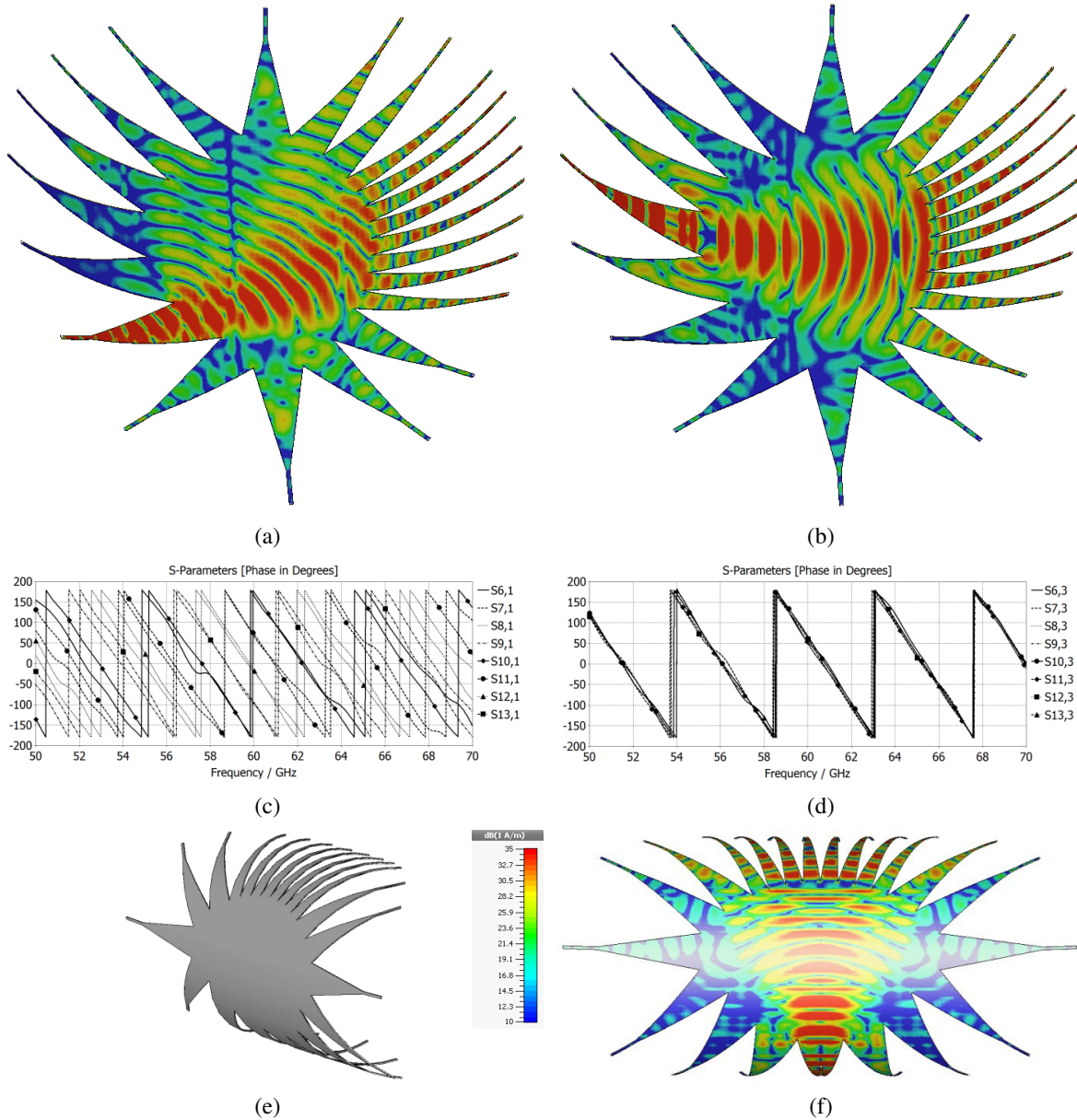
Figure 9. RF performance characteristics of the V-band LCP-based RL based on the flexural case of the convex-circumferential bending, in which the device is bent around cylinders of radiuses $R_1 = 20$-mm and $R_2 = 10$-mm: (a) surface current distributions for the excited port one; (b) surface current distributions for the excited port three; (c) linear phase behaviour for the excited port one; (d) linear phase behaviour for the excited port three; (e) extreme flexural structure of the lens; (f) surface current distributions for the excited beam port three under the extreme condition of the convex-circumferential bending.

4. DISCUSSION AND CONCLUSION

The paper presents the design, analysis, and performance evaluation of the V-band Rotman lens BFN based on the LCP substrate, along with conducting the comprehensive feasibility analysis of the flexible mm-wave beamformers for the potential employment in the flexible electronics and conformal wireless subsystems. The EM designs for the proposed flexures, including the concave-axial bending, convex-axial bending, concave-circumferential bending, and convex-circumferential bending, have been carried out, and the output performances in terms of the flexural structure, surface current distributions, linear phase behaviour required for the beam steering, and device efficiencies have been presented. The V-band Rotman lenses have confirmed the efficient maintenance of the output performance for the wideband operation. The demonstrated flexible lens-based beamformers are promising solutions in order to facilitate the deployment of the modern smart RF beam steering and to rank the deficient conventional services in the network infrastructures. The components exhibit significant features as the multi-environmental mm-wave beam-switching system cores for the conformal and irregular platforms at the network level with the interconnecting wireless backhaul links, in order to improve the system performance and radio coverage around the NAPs. The presented output characteristics of the core mm-wave lens component, as the high-performance fixed-weight beamformer, incorporate the intrinsic segments of the electronic beam scanning functionality, in order to apply the constant antenna weights (i.e., amplitude and phase) to the mm-wave array elements to effectively steer the main beam. Hence, the potential implementation of the V-band conformal antenna array; in the hybrid, integrated, distributed, or multilayer configurations; would result in the constructive spatial RF power distribution, based on the vector sum of the fields radiated by the individual antenna array elements and the AF exhibited by the distribution characteristics of the lens-based beamformer device, which is a function of the array geometry, and the amplitude and phase distributions applied to the individual elements of the antenna array [37]. The flexibility analysis can be further extended into the case of performance modelling and evaluation under the crumpling deformation condition (i.e., the combination of the proposed flexures) [38], along with the investigation of the spillover loss reduction mechanisms, in order to potentially decrease the sidewall reflections within the lens cavity, as well as increasing the device efficiency, for the appropriate implementation of the intended site-specific wireless subsystems, based on the RF beamforming techniques.

REFERENCES

1. Xu, F., et al., "Cylindrical conformal single-patch microstrip antennas based on three dimensional woven glass fiber/epoxy resin composites," *Composites Part B*, Vol. 78, 331–337, Sep. 2015.

2. Haghzadeh, M., H. M. Jaradat, C. Armiento, and A. Akyurtlu, "Design and simulation of fully printable conformal antennas with BST/polymer composite based phase shifters," *Progress In Electromagnetics Research C*, Vol. 62, 167–178, 2016.

3. Elias, N. A., et al., "Bending and crumpling deformation study of the resonant characteristic and SAR for a 2.4 GHz textile antenna," *Jurnal Teknologi*, Vol. 77, No. 10, 17–23, 2015.

4. Tang, M.-C., T. Shi, and R. W. Ziolkowski, "Flexible efficient quasi-Yagi printed uniplanar antenna," *IEEE Transactions on Antennas and Propagation*, Vol. 63, No. 12, 5343–5350, Dec. 2015.

5. Fan, K. K. and Z.-C. Hao, "Cylindrical conformal array antenna with tilted *H*-plane Fan-shaped beam for millimeter-wave application," *Microwave and Optical Technology Letters*, Vol. 58, No. 7, 1666–1671, Jul. 2016.

6. Semkin, V., et al., "Beam switching conformal antenna array for mm-wave communications," *IEEE Antennas and Wireless Propagation Letters*, Vol. 15, 28–31, Feb. 2016.

7. Saeed, S. M., C. A. Balanis, and C. R. Birtcher, "Inkjet-printed flexible reconfigurable antenna for conformal WLAN/WiMAX wireless devices," *IEEE Antennas and Wireless Propagation Letters*, 2016.

8. Hur, S., et al., "Millimeter wave beamforming for wireless backhaul and access in small cell networks," *IEEE Transactions on Communications*, Vol. 61, No. 10, 4391–4403, Oct. 2013.

9. Rappaport, T. S., et al., "Millimeter wave mobile communications for 5G cellular: It will work!," *IEEE Access*, Vol. 1, 335–349, May 2013.

10. Niu, Y., et al., "A survey of millimeter wave communications (mm Wave) for 5G: Opportunities and challenges," *Wireless Networks*, Vol. 21, No. 8, 2657–2676, Nov. 2015.

11. Zhu, Y., et al., "Demystifying 60GHz outdoor picocells," *20th Annual International Conference on Mobile Computing and Networking (MobiCom)*, 5–16, Sep. 2014.

12. Verma, L., M. Fakharzadeh, and S. Choi, "Backhaul need for speed: 60 GHz is the solution," *IEEE Wireless Communications*, Vol. 22, No. 6, 114–121, Dec. 2015.

13. Rahimian, A. and F. Mehran, "RF link budget analysis in urban propagation microcell environment for mobile radio communication systems link planning," *International Conference on Wireless Communications and Signal Processing (WCSP)*, 1–5, Nov. 2011.

14. Agiwal, M., A. Roy, and N. Saxena, "Next generation 5G wireless networks: A comprehensive survey," *IEEE Communications Surveys & Tutorials*, Vol. 18, No. 3, 1617–1655, Third Quarter, 2016.

15. Hall, P. S. and S. J. Vetterlein, "Review of radio frequency beamforming techniques for scanned and multiple beam antennas," *IEE Microwaves, Antennas and Propagation*, Vol. 137, No. 5, 293–303, Oct. 1990.

16. Rotman, W. and R. F. Turner, "Wide-angle microwave lens for line source applications," *IEEE Transactions on Antennas and Propagation*, Vol. 11, No. 6, 623–632, Nov. 1963.

17. Singhal, P. K, R. D. Gupta, and P. C. Sharma, "Recent trends in design and analysis of Rotman-type lens for multiple beamforming," *International Journal of RF and Microwave Computer-Aided Engineering*, Vol. 8, No. 3, 321–338, Feb. 1998.

18. Simon, P. S., "Analysis and synthesis of Rotman lenses," *22nd AIAA International Communications Satellite Systems Conference & Exhibit*, 1–11, May 2004.

19. Vashist, S., M. K. Soni, and P. K. Singhal, "A review on the development of Rotman lens antenna," *Chinese Journal of Engineering*, Vol. 2014, article ID 385385, 1–9, Jul. 2014.

20. Rahim, S. K. A. and P. Gardner, "A novel active antenna beamforming networks using Butler matrices," *Progress In Electromagnetics Research C*, Vol. 11, 183–198, 2009.

21. Song, I. S., et al., "60 GHz Rotman lens and new compact low loss delay line using LTCC technology," *IEEE Radio and Wireless Symposium (RWS)*, 663–666, Jan. 2009.

22. Lee, W., et al., "Compact two-layer Rotman lens-fed microstrip antenna array at 24 GHz," *IEEE Transactions on Antennas and Propagation*, Vol. 59, No. 2, 460–466, Feb. 2011.

23. Kushwah, R. P. S., P. K. Singhal, and P. C. Sharma, "Design of symmetric bootlace lens with gain analysis at UHF band," *Progress In Electromagnetics Research Letters*, Vol. 6, 83–89, 2009.

24. Lee, W., et al., "Beamforming lens antenna on a high resistivity silicon wafer for 60 GHz WPAN," *IEEE Transactions on Antennas and Propagation*, Vol. 58, No. 3, 706–713, Mar. 2010.

25. Rahimian, A., "Design and performance of a Ku-band Rotman lens beamforming network for satellite systems," *Progress In Electromagnetics Research M*, Vol. 28, 41–55, 2013.

26. Rajabalian, M. and B. Zakeri, "Optimisation and implementation for a non-focal Rotman lens design," *IET Microwaves, Antennas & Propagation*, Vol. 9, No. 9, 982–987, Jun. 2015.

27. Bhattacharyya, A. K., *Phased Array Antennas: Floquet Analysis, Synthesis, BFNs and Active Array Systems*, John Wiley & Sons, 2006.

28. Cho, C.-L., et al., "Inkjet-printed multilayer bandpass filter using liquid crystal polymer system-on-package technology," *IEEE Transactions on Components, Packaging and Manufacturing Technology*, Vol. 6, No. 4, 622–629, Apr. 2016.

29. Cabrol, P. and P. Pietraski, "60 GHz patch antenna array on low cost liquid-crystal polymer (LCP) substrate," *IEEE Long Island Systems, Applications and Technology Conference (LISAT)*, 1–6, May 2014.

30. Liu, D. and Y. P. Zhang, "Integration of array antennas in chip package for 60-GHz radios," *Proceedings of the IEEE*, Vol. 100, No. 7, 2364–2371, Jul. 2012.

31. Saily, J., et al., "Millimetre-wave beam-switching Rotman lens antenna designs on multi-layered LCP substrates," *10th European Conference on Antennas and Propagation (EuCAP)*, 1–5, Apr. 2016.

32. Kingsley, N., G. E. Ponchak, and J. Papapolymerou, "Reconfigurable RF MEMS phased array antenna integrated within a liquid crystal polymer (LCP) system-on-package," *IEEE Transactions on Antennas and Propagation*, Vol. 56, No. 1, 108–118, Jan. 2008.

33. Lamminen, A., et al., "Dual-circular polarised patch antenna array on LCP for 60 GHz millimetre-wave identification," *8th European Conference on Antennas and Propagation (EuCAP)*, 537–541, Apr. 2014.

34. Thompson, D. C., et al., "Characterization of liquid crystal polymer (LCP) material and transmission lines on LCP substrates from 30 to 110 GHz," *IEEE Transactions on Microwave Theory and Techniques*, Vol. 52, No. 4, 1343–1352, Apr. 2004.

35. Christie, S., et al., "Rotman lens-based retrodirective array," *IEEE Transactions on Antennas and Propagation*, Vol. 60, No. 3, 1343–1351, Mar. 2012.

36. Rotman, R., M. Tur, and L. Yaron, "True time delay in phased arrays," *Proceedings of the IEEE*, Vol. 104, No. 3, 504–518, Mar. 2016.

37. Kutty, S. and D. Sen, "Beamforming for millimeter wave communications: An inclusive survey," *IEEE Communications Surveys & Tutorials*, Vol. 18, No. 2, 949–973, Second Quarter, 2016.

38. Soh, P. J. and G. A. E. Vandenbosch, "Textile antennas for body area networks: design strategies and evaluation methods," *Electromagnetics of Body Area Networks: Antennas, Propagation, and RF Systems*, D. H. Werner and Z. H. Jiang (eds.), 1–25, John Wiley & Sons, Inc., 2016.